PCCP

Accepted Manuscript

ROYAL SOCIETY OF CHEMISTRY

www.rsc.org/pccp

Graphical Abstract

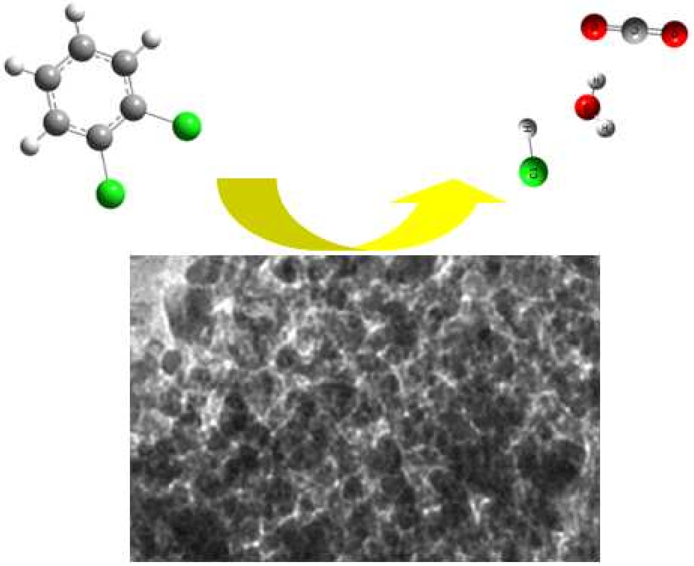

1,2-dichlorobenzene was completely oxidized to CO_2, H_2O and HCl over Ti-doped iron oxides at lower temperature with lower apparent activation energy.

Deep oxidation of 1,2-dichlorobenzene over Ti-doped iron oxide

Xiaodong Ma*[a], Xueyue Suo[a], Huiqin Cao[a], Jie Guo[a], Lu Lv[a], Hongwen Sun[a] and Meihua Zheng[a]

[a]Key Laboratory of Environmental Pollution Process and Standard, Ministry of Education, Tianjin Key Laboratory of Environmental Remediation and Pollution Control, College of Environmental Science and Engineering, Nankai University, Tianjin 300071, China

*Corresponding author: Tel.: +86-22-2350-1117; fax: +86-22-2350-1117; e-mail: maxd@nankai.edu.cn (X.D. Ma).

ABSTRACT

Ti-doped iron oxides with worm-like mesopores were successfully prepared using CTAB as the structure-directing agent. The as-prepared catalysts were characterized by XRD, Raman, H_2-TPR, XPS, TEM, and N_2 adsorption/desorption. The catalytic properties for oxidation of 1,2-dichlorobenzene (*o*-DCB) were investigated. The results showed that $Fe_{18}Ti_2O_x$ with 10 mol% Ti-doping shows the best catalytic activity, the total conversion of *o*-DCB can be obtained at 350°C. Moreover, $Fe_{18}Ti_2O_x$ exhibits higher stability, CO_2 selectivity and lower apparent activation energy. The high activity of $Fe_{18}Ti_2O_x$ could be ascribed to the combined factors including smaller crystallite size, excellent low-temperature reducibility, high surface active oxygen concentration and synergic effect between TiO_2 and mixed iron oxide (γ-Fe_2O_3 and α-Fe_2O_3). Acetate and formate species as intermediates were detected with in situ FTIR spectroscopy. A two-step redox mechanism of *o*-DCB decomposition on the surface of Ti-doped iron oxides was proposed. These results demonstrated that Ti-doped iron oxides could be developed as environmentally friendly catalysts for the deep oxidation of chlorinated volatile organic pollutants.

Keywords: Chlorinated volatile organic compounds; 1,2-dichlorobenzene; Catalytic oxidation; Ti-doped Fe_2O_3; Mechanism.

1. Introduction

Recently, Chlorinated volatile organic compounds (Cl-VOCs) have received widespread attention, due to their high toxicity and environmental persistence.[1-3] Catalytic oxidation of Cl-VOCs has been considered as one of the most promising technologies for the removing of Cl-VOCs compared with the traditional thermal destruction and adsorption, due to its lower reaction temperature, higher destruction efficiency, and lower selectivity to harmful byproducts.[4-8]

The catalysts for Cl-VOCs catalytic oxidation have been mainly focused on the two types of materials based on noble metals and transition metal oxides. Generally, noble metals exhibit higher low-temperature catalytic activity than transition metal oxides. However, the disadvantages of noble metal catalysts include: (a) higher costs, (b) deactivation due to HCl or Cl_2 poisoning, (c) chlorination of organic compounds besides oxidation.[9-12] Transition metal oxides can not only resist the deactivation resulting from the chlorine poisoning, but also enhance the catalytic performance by modifying composition and structure of oxides with some doping elements.[13-16] Various oxides have been studied as possible catalysts for Cl-VOCs decomposition: V_2O_5, Cr_2O_3, MoO_3, MnO_2 and Fe_2O_3.[17-23] Among them, Fe_2O_3-based catalysts have shown good application prospects in the elimination of Cl-VOCs, due to its advantages of high efficiency, low cost and environmental friendliness.[24,25] Interestingly, Fe_2O_3 supported on TiO_2 exhibited better catalytic activity than pure Fe_2O_3 catalysts.[26,27] The enhanced catalytic performance of TiO_2-Fe_2O_3 composite oxides could be attributed to the combined effects of high affinity of Ti^{4+} sites to adsorb Cl-VOCs and excellent oxidation role of Fe_2O_3.[26] While further researches have proved that pure TiO_2 has lower activity for the catalytic oxidation of Cl-VOCs,[28] suggesting TiO_2 is not suitable for acting as main active component in the TiO_2-Fe_2O_3 catalytic system.

Previous studies reveal the existence of strong interface interaction between TiO_2 and Fe_2O_3. However, overall and deep insight into this catalytic system is lack. It is thus necessary to regulate the composition and structure of the TiO_2-Fe_2O_3 catalyst to develop an efficient low-temperature catalytic oxidation technology for Cl-VOCs.

This paper presents the study results on the activity of Ti-doped Fe_2O_3 with worm-like mesopores for the total oxidation of *o*-DCB, used as a model compound of Cl-VOCs. The objectives of this study include: (i) developing an effective, environmentally friendly catalyst for the deep oxidation of Cl-VOCs, (ii) evaluating the effect of the reaction parameters such as reaction temperature and atmosphere on the catalytic performance, (iii) examining the structure-reactivity relationship in the Ti-doped Fe_2O_3 system, (iv) investigating the stability, reaction kinetics and intermediate products, (v) understanding the oxidative decomposition mechanism of Cl-VOCs on the Ti-doped Fe_2O_3.

2. Results and discussion

2.1. Characterization of catalysts

In order to investigate the thermal conversion characteristics of the as-prepared catalyst precursor, TGA of $Fe_{18}Ti_2O_x$ was performed and the corresponding TG curve is presented in Fig.1. It can be seen clearly that the TGA curve presents a continuous weight loss (39.44%) from room temperature to 500°C, which attributes to the decomposition of the catalyst precursor into $Fe_{18}Ti_2O_x$. Considering the weight of catalyst almost remains constant above 500°C, and avoiding the adverse effect of high temperature sintering for the catalytic activity, the calcination temperature of the catalyst is fixed at 500°C.

Fig. 2 shows the XRD patterns of the prepared catalysts with different composition after calcined at 500°C. The pure TiO_2 shows the characteristic diffraction peaks due to anatase TiO_2 (JCPDS 04-0477). Fe_2O_3 catalyst presents diffraction peaks at 2θ=30.3，35.6, and 63.0°, suggesting the existence of γ-Fe_2O_3 (JCPDS 04-0755). The diffraction peaks are observed at 2θ of 33.1, 40.9 and 49.5°, suggesting the presence of hematite α-Fe_2O_3 (JCPDS 33-0664). The mass percent of crystal phase of the catalysts is estimated by the normalized reference intensity ratio (RIR) method. It is noted that the relative content of γ-Fe_2O_3 varies with the increase of doping amount of Titanium. The mass ratio of γ-Fe_2O_3 to α-Fe_2O_3 is 66:34, 65:35, 86:14 and 73:27 for Fe_2O_3, $Fe_{19}TiO_x$, $Fe_{18}Ti_2O_x$

and $Fe_{17}Ti_3O_x$, respectively. This indicates that the doping of Ti^{4+} with appropriate amount (10mol%) improves the formation of γ-Fe_2O_3, leading to more γ-Fe_2O_3 is detected on the surface of $Fe_{18}Ti_2O_x$. The crystallite size of the catalyst is estimated by the Scherrer's equation. The average crystallite size of anatase TiO_2 is calculated to be about 22.9nm by using the peak (101) at $2\theta=35.6°$, the crystallite sizes of Fe_2O_3 and Ti-doped iron oxide are calculated by using the peak (311) of γ-Fe_2O_3 at $2\theta=35.6°$. The Crystallite size of Fe_2O_3 is 28.3nm. With the increase of doping concentration of Titanium, the crystallite size of Ti-doped iron oxide catalysts increases first and then decreases. Crystallite size values of Ti-doped iron oxide catalysts are 38.1, 14.9 and 26.2nm for $Fe_{19}TiO_x$, $Fe_{18}Ti_2O_x$ and $Fe_{17}Ti_3O_x$, respectively. No diffraction peaks corresponding to any titanium oxide or iron-titanium oxide species can be distinguished in the diffractograms of $Fe_{19}TiO_x$, $Fe_{18}Ti_2O_x$ and $Fe_{17}Ti_3O_x$. One possible explanation is that titanium oxide particles are highly dispersed on the surface of iron oxide with very small particle sizes; another possible reason is the diffusion of Ti^{4+} into the lattice of iron oxide, as the radius of Fe^{3+} (0.55Å) is quite close to that of Ti^{4+} (0.60Å).[29]

To further study the effect of Ti doping on the crystal structure, Raman spectroscopy investigation was conducted. Fig. 3 shows the Raman spectra collected on the synthesized catalysts. For the undoped Fe_2O_3 catalyst, Raman bands at 220, 290 and 408cm^{-1} correspond respectively to hematite's A_{1g}, E_g, E_g modes,[30] and 342, 504, 667 and 714cm^{-1} correspond respectively to maghemite's E_g, T_{2g}, A_{1g}, A_{1g} modes.[30] The Raman spectra of TiO_2 is characterized by a strong band at 140 cm^{-1}, three middle intensity bands at 390, 508 and 633cm^{-1}. These peaks can be attributed to the fundamental vibration modes of anatase TiO_2 with the symmetries of E_g, B_{1g}, A_{1g} and $E_{g,}$ respectively.[31,32] These results are consistent with the XRD measurements. As can be seen from the Raman patterns, the intensities of Raman bands of Ti-doped iron oxides are significantly different from those of iron oxides, which could be ascribed to the modification of the structure of iron oxides by the Ti doping. It is noteworthy that, only on the $Fe_{18}Ti_2O_x$ surface, the E_g mode (140cm^{-1}) of anatase TiO_2 coexists with the vibration modes of hematite and maghemite, suggesting that Ti doping with appropriate amount leads to the coexistence of anatase TiO_2, α-Fe_2O_3 and γ-Fe_2O_3 on the surface of the catalyst.

The reducibility of the catalyst is a very important parameter which can affect the catalytic performance. In Fig. 4, the reducibility of $Fe_{18}Ti_2O_x$ is compared to that of TiO_2 and Fe_2O_3 as reference. H_2-TPR of individual TiO_2 shows poorly identified peaks at 570°C, indicating that TiO_2 is difficult to be reduced even at relatively higher temperature. For Fe_2O_3, the peak centered at 487°C can be assigned to the reduction of Fe_2O_3 to Fe_3O_4, whereas the peak at 568°C is attributed to the transformations of Fe_3O_4 to FeO, and the third peak at 712°C is assigned to the reduction of FeO to Fe.[25,33,34] With the addition of Ti into Fe_2O_3, the reduction peaks of $Fe_{18}Ti_2O_x$ are shifted towards higher temperatures. Obviously, the addition of Ti into Fe_2O_3 leads to the significant increase in H_2 consumption corresponding to the peak between 325 and 555°C, suggesting that there is a strong interaction between TiO_2 and Fe_2O_3. The hydrogen consumption is 7.95×10^{-6} mmol for TiO_2 in the temperature range of 325-630 °C, 6.44×10^{-5} mmol for Fe_2O_3 in the temperature range of 325-610 °C, 1.08×10^{-4} mmol for $Fe_{18}Ti_2O_x$ in the temperature range of 325-555 °C. The above results indicate that when temperature is lower than 630 °C, hydrogen consumption decreased in the order of $Fe_{18}Ti_2O_x > Fe_2O_3 > TiO_2$. Considering the catalysts show the catalytic activities, even when temperature is lower than 325 °C (shown in Fig. 8), it is more meaningful to further compare the low-temperature reducibility of the TiO_2, Fe_2O_3 and $Fe_{18}Ti_2O_x$, before the occurrence of phase transformation. For this purpose, initial H_2 consumption rate of the first peak of each sample was calculated,[15] as shown in Fig. 4b. It is clear that the initial H_2 consumption rate decreases in the following order: $Fe_{18}Ti_2O_x > Fe_2O_3 > TiO_2$. Compared with the catalytic performances shown in Fig. 8, it could be deduced that the low-temperature reducibility of prepared catalysts reflects the catalytic performance of the synthesized counterparts.

The surface chemical components and electronic state of Fe_2O_3 and

$Fe_{18}Ti_2O_x$ were investigated by X-ray photoelectron spectroscopy (XPS). As seen in Fig. 5a, the peaks centered at 464.2 and 458.3eV are observed on the surface of $Fe_{18}Ti_2O_x$ catalyst, which can be attributed to Ti $2p_{1/2}$ and Ti $2p_{3/2}$ of Ti (IV) oxidation state, respectively.[35,36] Fig. 5b illustrates the O 1s XPS spectra of Fe_2O_3 and $Fe_{18}Ti_2O_x$, as shown in Fig. 5b, the asymmetrical O 1s signal of the catalysts could be deconvoluted to three components: lattice oxygen (O_{latt}) at 529-530eV, surface active oxygen (O_{sur}) at 531-532 eV and adsorbed oxygen species (O_{ads}) at 533-534eV.[11] The calculated $O_{sur}/(O_{latt}+O_{sur}+O_{ads})$ molar ratios of Fe_2O_3 and $Fe_{18}Ti_2O_x$ are 0.32 and 0.48, respectively. It is well known that the high O_{sur} concentration is beneficial for the activity of catalytic oxidation.[15] This may give another reasonable explanation for the high activity of $Fe_{18}Ti_2O_x$ in the following activity tests.

The typical TEM images of the prepared $Fe_{18}Ti_2O_x$ are shown in Fig. 6. From Fig. 6a and b, homogeneous worm-like mesopores resulting from the intergranular cavities of the sample can be clearly observed. Previous researches have revealed that when CTAB is introduced into the synthetic process as a template, a large number of interstices among catalyst nanoparticles are created, this result can increase the reactive sites of the catalyst and improve the catalytic activity.[23] The high-resolution TEM (HRTEM) image shown in Fig. 6c reveals the interplanar spacing of 0.36nm for the (012) plane of α-Fe_2O_3

nanoparticles and that of 0.25nm for the (311) plane of γ-Fe_2O_3. nanoparticles, demonstrating that the α-Fe_2O_3 and γ-Fe_2O_3 coexist in the catalyst, which are in good agreement with the XRD results. Selected area electron diffraction analysis (Fig. 6d) shows discrete diffraction spots and diffraction ring, which indicates the existence of single-crystalline and polycrystalline phase on the $Fe_{18}Ti_2O_x$ surface.

To understand the structure of the synthesized catalysts in detail, FeCa10 catalyst was taken as representative for further characterization. Fig. 7 shows the nitrogen adsorption/desorption isotherms and the derived pore size distributions of the synthesized $Fe_{18}Ti_2O_x$. The specific surface area, total pore volume and average pore diameter were 65.3m^2/g, 0.25cm^3/g and 14.8nm, respectively. The isotherm exhibits a type IV curve with a H1 type hysteresis loop at the relative pressure P/P_0 in the range of 0.6–1.0. This characteristic agrees well with that of mesoporous material reported in the previous literature.[37]

2.2. Activity measurements

Fig.8 shows catalytic performance for *o*-DCB oxidation over different catalysts. It is noted that the *o*-DCB conversion over Fe_2O_3, TiO_2 and $Fe_{17}Ti_3O_x$ first increases, then decreases reaching the minimum at 200°C, and finally starts to increase again. The first increase and decrease of *o*-DCB conversion could be mainly attributed to the adsorption and thermal desorption of *o*-DCB, respectively. The second increase of *o*-DCB conversion could be ascribed to the oxidation degradation of *o*-DCB. Similar catalytic behavior has also been reported in the catalytic oxidation of chlorobenzene over MnO_x-CeO_2 catalysts[10]. The *o*-DCB conversion over $Fe_{19}TiO_x$ decreases from 100 to 200°C, corresponding to the thermal desorption stage. The common characteristics exhibited in the light-off curves of the above four catalysts are the oxidation degradation of *o*-DCB are all initiated at 200°C. It is interesting to note that the catalytic behavior of $Fe_{18}Ti_2O_x$ is significantly different from the other catalysts, the *o*-DCB conversion over $Fe_{18}Ti_2O_x$ increases continuously with the rise of temperature. The different catalytic activities of these catalysts could be related to different nature of various catalysts. It can be seen from Fig.8 that the catalytic activity of pure Fe_2O_3 is significantly higher than that of pure TiO_2. At 350°C, *o*-DCB conversion can reach 99.2%. However, the catalytic activity of pure Fe_2O_3 is lower in the low temperature range, the *o*-DCB conversion is only 29.7% at 250°C. The doping amount of Ti has an important influence on the catalytic activity of iron oxide. Compared with other catalysts, $Fe_{18}Ti_2O_x$ with 10mol% Ti-doping shows best catalytic activity for *o*-DCB conversion. The total conversion of *o*-DCB can be obtained at 350°C. In the low temperature (< 350 °C) range, the activity is significantly higher than that of other catalysts, such as *o*-DCB conversion is up to 89.6% at 250°C. The enhanced activity of $Fe_{18}Ti_2O_x$ catalyst can be attributed to the following two factors: i) the formation of more γ-Fe_2O_3 with smaller crystallite size on the surface of the catalyst,[38] which has been confirmed by the XRD and Raman analyses. ii) the synergic interaction between iron oxide and titanium oxide. In the previous work, it has been proved that γ-Fe_2O_3 exhibits better low-temperature activity for the oxidation of Cl-VOCs than α-Fe_2O_3.[25] In this study, the analytical results of initial H_2 consumption rate show that low-temperature reducibility of $Fe_{18}Ti_2O_x$ is higher than pure Fe_2O_3, which might be related to the formation of more γ-Fe_2O_3 due to the doping of proper amount of Titanium. Besides, the high activity of $Fe_{18}Ti_2O_x$ is also associated with smaller crystallite size of γ-Fe_2O_3 nanoparticles. Size-dependent catalytic activity has been reported in the previous studies. Generally, smaller crystallite size leads to more crystalline defects, more active surface sites and higher catalytic performance.[39] Previous studies have showed that Fe-Ti composite oxides have excellent catalytic activity for the oxidation of chlorinated hydrocarbons at relatively low temperatures. Khaleel e al.[26] reported that Fe–Ti-oxide catalyst exhibited high activity and showed a promising catalytic potential for the complete oxidation of chlorobenzene, which could be attributed to the synergic interaction between α-Fe_2O_3 and TiO_2 active phases. It is proposed that high affinity of Ti^{4+} sites to adsorb chlorobenzene is an important factor that contribute to the enhanced activity of Fe–Ti-oxide catalyst.[26]

2.3. Effect of the dosage of CTAB on the catalytic activity

To discuss the effect of different dosages of CTAB in the preparation process on the catalytic activities, Ti-doped iron oxides with a Fe : Ti molar ratio of 18 : 2 were taken as representative catalysts for further test. The dosage of CTAB in the preparation is 0, 9 and 18mmol, respectively. As depicted in Fig. 9, the dosage of CTAB has a significant influence on the catalytic activity of Ti-doped iron oxides. The activity of the catalyst without adding CTAB is so low that *o*-DCB conversion is only 44.8% at 500°C. When 9mmol CTAB is added, the activity of $Fe_{18}Ti_2O_x$ increases dramatically, the complete conversion of *o*-DCB can be obtained at 350°C. However, When the dosage of CTAB is further increased to 18mmol, the activity of the catalyst substantially decreases. CTAB as template has been used for the synthesis of mesoporous metal oxides. It is revealed that CTAB plays a key role in controlling the morphologies of the synthesized oxides. Liu et al.[40] reported that mesoporous NiO synthesized with CTAB showed good thermal stability and high surface area. In this case, $Fe_{18}Ti_2O_x$ with worm-like mesoporous structure exhibited the highest catalytic activity, which could be related to the surface modification and morphological control of proper amount of CTAB.

2.4. Effect of oxygen concentration on *o*-DCB conversion

The effect of oxygen concentration on the conversion of *o*-DCB over

$Fe_{18}Ti_2O_x$ catalyst is also investigated, the results are shown in Fig. 10. It can be seen that the conversion of *o*-DCB takes place even in the absence of gas-phase oxygen, indicating that surface lattice oxygen of the catalyst is likely involved in the *o*-DCB oxidation. However, *o*-DCB conversion is considerably lower than those when oxygen is presence. The value is only 62.7% under oxygen-free condition at 350°C. When 10% O_2 is introduced in the feed, the *o*-DCB conversion can be significantly improved, the total conversion rate of *o*-DCB is reached at 350°C, which is 37.3% higher than that without O_2. This suggests that O_2 should play an important role in the catalytic oxidation of *o*-DCB. Previous work has also shown that the presence of gaseous oxygen benefited the regeneration of catalyst surface and also improved the formation rate of oxidation products on the catalyst surface.[28] The further investigation discovers that 10% O_2 is sufficient for the conversion of *o*-DCB, when O_2 concentration increases to 20%, the change of *o*-DCB conversion is not obvious. It can be deduced that O_2 molecular mainly takes part in the reaction through activating or regenerating the active oxygen species located in the vacancies of the catalyst surfaces, instead of participating the reaction with *o*-DCB directly.

2.5. Catalyst stability

From the viewpoint of practical application, it is very important to evaluate the stability of the catalyst. Previous work has reported that the formed HCl or Cl_2 may cause the rapid deactivation of catalysts used for the catalytic decomposition of Cl-VOCs.[19] In this study, the experiments for stability test over $Fe_{18}Ti_2O_x$ catalyst were carried out by feeding the stream containing 100 ppm *o*-DCB and 10% O_2 at 350°C at space velocity 22,000h^{-1}. As shown in Fig. 11, stable activity over $Fe_{18}Ti_2O_x$ is observed without an obvious decrease in *o*-DCB conversion. $Fe_{18}Ti_2O_x$ keeps better stability even after continuous reaction for 630 minutes, with *o*-DCB conversion being 97.5%. In our previous work, It has been reported that the catalytic stability of iron oxide can be improved be doping of metal cations.[41] The doped metal cations can improve the Cl^- exchange and regenerate the active sites on the iron oxide, leading to the higher catalytic stability.

To investigate the change in chemical states of the elements and adsorbed species on the $Fe_{18}Ti_2O_x$ surface after reaction, the used $Fe_{18}Ti_2O_x$ was analyzed by XPS. XPS results, shown in Fig. 12a, indicate that the binding energies of Fe 2p for $Fe_{18}Ti_2O_x$ remain almost unchanged after the reaction. Considering iron oxide is the main active component of the $Fe_{18}Ti_2O_x$, it can be deduced that high catalytic stability of $Fe_{18}Ti_2O_x$ is related to the high stability of the chemical states of iron species on the $Fe_{18}Ti_2O_x$. The C 1s XPS spectra shown in Fig. 12b reveal that, after reaction, no obvious residual carbonaceous species was detected, which is undoubtedly beneficial for keeping the long-term and efficient catalytic activity. While as shown in Fig. 12c and Fig. 12d, O1s and Cl 2p XPS spectra of the used $Fe_{18}Ti_2O_x$ exhibit different characteristics, compared with those of the fresh catalyst. It can be seen from Fig. 12c that, after reaction, XPS peak positions of O_{sur} and O_{ads} remain unchanged, while the peak of O_{latt} shifts from 529.8 to 529.9eV. The $O_{sur}/(O_{latt}+O_{sur}+O_{ads})$ molar ratio of $Fe_{18}Ti_2O_x$ decreases from 0.48 to 014, suggesting that surface active oxygen species participates in the catalytic oxidation of *o*-DCB and is consumed after a long-time reaction. A weak Cl $2p_{3/2}$ peak at 198.6eV is observed in on the XPS spectrum of the used $Fe_{18}Ti_2O_x$ catalyst (Fig. 12d), indicating the presence of residual chlorine species on the used $Fe_{18}Ti_2O_x$ catalyst. According to the analytical results of Fig. 12c and Fig. 12d, the conclusion can be drawn that the decrease of O_{sur} concentration and the Cl^- residues might be the main factors leading to the slight deactivation of the catalyst. On the other hand, the appearance of residual Cl^- also provides the evidence of the mineralization of organic chlorine into chloride ions.

2.6. Kinetic studies

Due to the fact that $Fe_{18}Ti_2O_x$ exhibits higher catalytic activity and stability, the kinetic study of catalytic oxidation of *o*-DCB over $Fe_{18}Ti_2O_x$ was carried out in the temperature range of 100–250°C. Considering the concentration of O_2 is far above that of *o*-DCB and supposing the catalytic oxidation of *o*-DCB is first-order reaction, yields the following kinetic expression:

$$\ln[1/(1-X)]=k_{ap}\ \tau \qquad (2)$$

where X is *o*-DCB conversion, k_{ap} is the apparent rate constant of the reaction, τ is the space time (s), and is defined as the reciprocal of the space velocity. Fig. 13 shows the plot of $\ln[1/(1-X)]$ versus τ for the catalytic oxidation of *o*-DCB over $Fe_{18}Ti_2O_x$ catalyst with the correlation coefficient (R^2) of 0.986 and 0.999 at 100 and 250°C, respectively. The results indicate a straight-line relationship between $\ln[1/(1-X)]$ and τ, validating the assumption that catalytic oxidation of *o*-DCB follows a first-order rate law. A straight line plot of $\ln[1/(1-X)]$ versus τ yields the slope of k_{ap}. The apparent rate constants of *o*-DCB conversion at 373K and 523K are k_{ap1}=0.01447s^{-1} and k_{ap2}=0.08677s^{-1}, respectively. The apparent activation energy of the catalytic oxidation of *o*-DCB over $Fe_{18}Ti_2O_x$ was calculated based on the Arrhenius equation (Eq. (3)). The calculated value is about 19.37kJ/mol.

$$\ln\frac{k_{ap1}}{k_{ap2}}=\frac{E_a}{R}\left(\frac{1}{T_2}-\frac{1}{T_1}\right) \qquad (3)$$

where k_{ap1} and k_{ap2} are the apparent rate constants at 373K and 523K, respectively, s^{-1}; E_a is the apparent activation energy, kJ/mol; and T_1 and T_2 are the reaction temperatures, K. The apparent activation energy in this study is significantly lower than the value in the catalytic oxidation of *o*-DCB over V_2O_5/TiO_2-based catalysts (29-37kJ/mol),[42] and those in the catalytic oxidation of *o*-DCB over V_2O_5/TiO_2 and $V_2O_5/MoO_3–TiO_2$

(34.4 and 31.5kJ/mol).[43] These results suggest an obvious advantage of kinetics in the catalytic oxidation of Cl-VOCs over $Fe_{18}Ti_2O_x$.

2.7. In situ FTIR studies

In order to obtain deep insights into the reaction mechanism, the process of dissociative adsorption of *o*-DCB over $Fe_{18}Ti_2O_x$ catalyst was studied by means of in situ FTIR spectroscopy. FTIR spectra collected at different time intervals during *o*-DCB adsorption and oxidation over $Fe_{18}Ti_2O_x$ at 250°C are shown in Fig. 14a. FTIR spectra collected at different temperatures after 10 min reaction are shown in Fig. 14b. The band at $1457cm^{-1}$ (νCOO^- asym), with an adjoining shoulder at $1432cm^{-1}$ (νCOO^- sym), can be assigned to the carboxylates of the acetate type.[44] The weak peaks at $1578cm^{-1}$ (νCOO^- sym) indicates the formation of surface formate species.[45] The band at $1649cm^{-1}$ can be attributed to superimposed bands due to ν(C=O)-stretching vibrations of formic acid and δ(HOH) modes of adsorbed water.[46] The peaks at 2339 and $2361cm^{-1}$ are ascribed to CO_2 species.[47] The broad bands between 3400-$3900cm^{-1}$ can be attributed to formed water on the surface of $Fe_{18}Ti_2O_x$.[23] With the extension of reaction time and the increase of reaction temperature, it is clear that the intensities of the bands corresponding to surface carboxylates decrease, while those of CO_2 and H_2O increase gradually. These results indicate that carboxylate species are not the stable species in the oxidation over $Fe_{18}Ti_2O_x$, they tend to decompose quickly into CO_2

and H_2O, which are the final products of deep oxidation of the *o*-DCB.

2.8. Reaction mechanism of *o*-DCB oxidation over Ti-doped iron oxide

As seen in Fig. 15, the catalytic oxidation of *o*-DCB over $Fe_{18}Ti_2O_x$ occurs via a two-step process: in the first step, Cl is abstracted from *o*-DCB by the nucleophilic substitution of the surface oxygen species, forming surface phenolates; in the second step, the remaining aromatic ring is oxidized, forming partial oxidation intermediates (carboxylates) which can be further oxidized to form CO_2, H_2O and HCl. Since no peaks corresponding to C–Cl vibrations were observed by in situ FTIR spectra, suggesting the abstraction of the Cl atom may well be a fast step.

3. Experimental

3.1. Catalyst preparation

All chemicals were of analytical grade and used as received without further purification. In the Ti-doped Fe_2O_3 synthesis procedure, cetyltrimethylammonium bromide (CTAB) was dissolved into 300mL deionized water in required quantities. After stirring for 0.5h, $Fe(NO_3)_3·9H_2O$ and $TiOSO_4$ were dissolved into the above solution with suitable ratios under magnetic stirring. Then 0.2mol/L of NaOH aqueous solution was gradually added to reach the pH to around 10 and continued stirring for 12h. The suspended solution was put into water bath at 80°C, until the water was completely vaporized, and then washed with deionized water and ethanol in sequence, dried at 80°C for 6h, then calcined at 500°C for 3h to produce Ti-doped Fe_2O_3. The catalysts with Fe/Ti molar ratio of 19:1, 18:2 and 17:3 were denoted as $Fe_{19}TiO_x$, $Fe_{18}Ti_2O_x$ and $Fe_{17}Ti_3O_x$. For comparison, pure Fe_2O_3 and TiO_2 have also been synthesized with the same procedure.

3.2. Catalyst characterization

The powder X-ray diffraction patterns (XRD) were recorded on a Rigaku D/max-2500 powder diffractometer using Cu Ka radiation (40kV and 100mA). Crystal phases were identified by referring the diffraction peaks to those of standard compounds reported in the JCPDS Data File. The Raman spectra were obtained with a Renishaw inVia spectrometer using laser excitation at 514.5nm. Hydrogen temperature-programmed reduction (H_2-TPR) experiments were carried out in the RT-900°C range on a Thermo-Finnigan TPDRO 1100 instrument with a heating rate of 10°C/min and a flow rate of 5vol% H_2/Ar (40mL/min). Hydrogen consumption was monitored by a thermal conductivity detector. X-ray photoelectron spectra (XPS) were performed with a Kratos Axis Ultra DLD spectrometer employing a monochromated Al-Kα X-ray source (hν=1,486.6eV), 150W, hybrid (magnetic/electrostatic) optics, multi-channel plate and delay line detector. The recorded XPS spectra were charge corrected with respect to the C1s peak at 284.6eV. Transmission electron microscopy (TEM) and high-resolution transmission electron microscopy (HRTEM) images were conducted on a

TECNAI G^2 F20 microscope operated at an accelerating voltage of 200kV. The sample was dispersed in ethanol and treated with ultrasound for 5min, and then deposited on a copper grid coated with preformed holey carbon film. Specific surface area and pore volume measurements were measured by N_2 physisorption at 77K using a Quantachrome NOVA 2000e sorption analyzer. Prior to N_2 physisorption, the samples were outgassed in vacuum during 6h at 200°C

3.3. Catalytic test

Catalytic tests were performed in a continuous-flow fixed-bed microreactor operating at atmospheric pressure. Each run used approximately 200mg of catalyst with 120–180 mesh particles. The gas stream was composed of 100ppm of *o*-DCB, 10 vol.% of O_2 and helium as diluting gas to obtain 60mL/min. A typical gas hourly space velocity (GHSV) was 22,000h^{-1}. Catalytic tests were run from 100 to 500°C. After 30min reaction, the reactants and products were analyzed on-line by a GC1100 gas chromatograph equipped with a flame ionization detector (FID) and a 3.0m stainless steel column packed with GDX103 (60/80 mesh). The activity was expressed as the conversion of *o*-DCB, calculated by the following equation:

$$X(\%) = (1 - \frac{C_{out}}{C_{in}}) \times 100\% \qquad (1)$$

Where C_{in} is the initial concentration of *o*-DCB before reaction, C_{out} is the final concentration of *o*-DCB after reaction.

3.4. Kinetic studies

Each *o*-DCB catalytic oxidation test conducted in this study was under isothermal operation. The effect of the concentrations of the reactants on the rate of *o*-DCB oxidation was investigated in the range of 100–250°C. The mass of the catalyst was fixed at 200mg, the total flow rate of the gaseous mixture flowing through the catalytic reactor was 60 mL/min, the concentration of *o*-DCB was varied by changing *o*-DCB flow rate from 0.5 to 2.5mL/min.

3.5. In-situ FTIR studies

In-situ FTIR spectra were recorded using a PerkinElmer 2000 FT-IR spectrophotometer with a resolution of 2cm^{-1}. The catalysts were in the form of self-supporting thin discs of about 25mg/cm^2 and 0.1mm thick. The samples were placed in a holder and kept in the middle of the IR cell. Before each experiment, catalyst samples were pretreated in vacuum at 350°C for 1h and then cooled to room temperature or desired temperature, and spectra of the clean catalyst were collected and utilized as the background. In order to investigate the dissociative adsorption of *o*-DCB on the surface of the catalyst, *o*-DCB vapor was introduced into the cell in a mixture of 10% O_2/N_2. In-situ FTIR spectra were collected at different time intervals until a steady state was reached.

4. Conclusions

Ti-doped iron oxides were prepared and tested as catalysts for the oxidation of *o*-DCB. $Fe_{18}Ti_2O_x$ with 10mol% Ti-doping shows the best catalytic activity, higher stability and CO_2 selectivity, and lower apparent activation energy. The high activity of $Fe_{18}Ti_2O_x$ could be attributed to the small crystallite size, high surface active oxygen concentration, good low-temperature reducibility and synergic effect between TiO_2 and mixed iron oxide, in which γ-Fe_2O_3 predominates. In situ FTIR studies indicate the acetate and formate species are intermediates of the oxidation process. The decomposition of *o*-DCB on the surface of $Fe_{18}Ti_2O_x$ involves a two-step redox process. These experimental results have shown that Ti-doped iron oxides can be potentially applied as low-cost and environmentally friendly catalysts for the deep oxidation of Cl-VOCs.

Acknowledgments

The authors gratefully acknowledge financial support for this work from National Natural Science Foundation of China (No. 21177066, 41225014 and 31370700), the Science and Technology Commission Foundation of Tianjin (No. 11JCYBJC05100), Program for New Century Excellent Talents in University (NCET-12-0284).

References

1 K. L. Froese, O. Hutzinger, *Environ. Sci. Technol.,* 1996, **30**, 998-1008.

2 H. Duan, J. Li, Y. Liu, N. Yamazaki, W. Jiang, *Environ. Sci. Technol.,* 2011, **45**, 6322-6328.

3 C. Gannoun, A. Turki, H. Kochkar, R. Delaigle, P. Eloy, A. Ghorbel, E.

M. Gaigneaux, *Appl. Catal. B,* 2014, **147**, 58–64.

4 J. Lichtenberger, M. D. Amiridis, *J. Catal.,* 2004, **223**, 296-308.

5 Y. Fan, X. Lu, Y. Ni, H. Zhang, L. Zhao, J. Chen, C. Sun, *Environ. Sci. Technol.,* 2010, **44**, 3079-3084.

6 Y. Fan, X. Lu, Y. Ni, H. Zhang, M. Zhu, Y. Li, J. Chen, *Appl. Catal. B,* 2011, **101**, 606-612.

7 Y. Dai, X. Wang, Q. Dai, D. Li, *Appl. Catal. B,* 2012, **111–112**, 141-149.

8 S. Lin, G. Su, M. Zheng, D. Ji, M. Jia, Y. Liu, *Appl. Catal. B,* 2012, **123–124**, 440–447.

9 S. H. Chang, K. H. Chi, C. W. Yong, B. Z. Hong, M. B. Chang, *Environ. Sci. Technol.,* 2009, **43**, 7523-7530.

10 X. Wang, Q. Kang, D. Li, *Appl. Catal. B,* 2009, **86**, 166-175.

11 Y. Dai, X. Wang, D. Li, Q. Dai, *J. Hazard. Mater.,* 2011, **188**, 132–139.

12 W. Zhao, J. Cheng, L. Wang, J. Chu, J. Qu, Y. Liu, S. Li, H. Zhang, J. Wang, Z. Hao, T. Qi, *Appl. Catal. B,* 2012, **127**, 246-254.

13 C. E. Hetrick, J. Lichtenberger, M. D. Amiridis, *Appl. Catal. B,* 2008, **77**, 255-263.

14 X. Ma, H. Sun, Q. Sun, X. Feng, H. Guo, B. Fan, S. Zhao, X. He, L. Lv, *Catal. Commun.,* 2011, **12**, 426-430.

15 F. Wang, H. Dai, J. Deng, G. Bai, K. Ji, Y. Liu, *Environ. Sci. Technol.,* 2012, **46**, 4034–4041.

16 X. Ma, X. Feng, X. He, H. Guo, L. Lv, J. Guo, H. Cao, T. Zhou, *Micropor, Mesopor. Mater.,* 2012, **158**, 214-218.

17 R. Weber, T. Sakurai, H. Hagenmeier, *Appl. Catal. B,* 1999, **20**, 249-256.

18 S. Krishnamoorthy, J. A. Rivas, M. D. Amiridis, *J. Catal.,* 2000, **193**, 264–272.

19 Y. Liu, M. F. Luo, Z. B. Wei, Q. Xin, P. L. Ying, C. Li, *Appl. Catal. B,* 2001, **29**, 61-67.

20 M. A. Larrubia, G. Busca, *Appl. Catal. B,* 2002, **39**, 343-352.

21 S. Albonetti, S. Blasioli, R. Bonelli, J. E. Mengou, S. Scirè, F. Trifirò, *Appl. Catal. A,* 2008, **341**, 18-25.

22 C. E. Hetrick, J. Lichtenberger, M. D. Amiridis, *Appl. Catal. B,* 2008, **77**, 255-263.

23 X. Ma, Q. Sun, X. Feng, X. He, J. Guo, H. Sun, H. Cao, *Appl. Catal. A,* 2013, **450**, 143-151.

24 S. Chin, J. Jurng, J. H. Lee, S. J. Moon, *Chemosphere,* 2009, **75**, 1206-1209.

25 S. Lomnicki, B. Dellinger, *Environ. Sci. Technol.,* 2003, **37**, 4254-4260.

26 A. Khaleel, A. Al-Nayli, *Appl. Catal. B,* 2008, **80**, 176-184.

27 H. C. Wang, H. S. Liang, M. B. Chang, *J. Hazard. Mater.,* 2011, **186**, 1781-1787.

28 X. Ma, J. Shen, W. Pu, H. Sun, Q. Pang, J. Guo, T. Zhou, H. Cao, *Appl. Catal. A,* 2013, **466**, 68-76.

29 P. Sharma, P. Kumar, A. Solanki, R. Shrivastav, S. Dass, V. R. Satsangi, *J. Solid State Electr.,* 2012, **16**, 1305-1312.

30 M. A. Legodi, D. de Waal, *Dyes Pigments,* 2007, **74**, 161-168.

31 P. R. Ettireddy, N. Ettireddy, S. Mamedov, P. Boolchand, P. G. Smirniotis, *Appl. Catal. B,* 2007, **76**, 123-134.

32 Y. Wu, J. Zhang, L. Xiao, F. Chen, *Appl. Catal. B,* 2009, **88**, 525-532.

33 S. Minicò, S. Scirè, C. Crisafulli, R. Maggiore, S. Galvagno, *Appl. Catal. B,* 2000, **28**, 245-251.

34 S. Gaur, S. Johansson, F. Mohammad, C. S. S. R. Kumar, J. J. Spivey, *J. Phys. Chem. C,* 2012, **116**, 22319−22326.

35 S. S. Thind, G. Wu, A. Chen, *Appl. Catal. B,* 2012, **111-112**, 38-45.

36 F. Li, X. Wang, Y. Zhao, J. Liu, Y. Hao, R. Liu, D. Zhao, *Appl. Catal. B,* 2014, **144**, 442-453.

37 K. S. W. Sing, D. H. Evrett, R. A. W. Haul, L. Moscou, R. A. Pierotti, J. Rouquerol, T. Siemieniewska, *Pure Appl. Chem.,* 1985, **57**, 603-619.

38 H. Li, L. Li, Y. Li, *Nanotechnol. Rev.*, 2013, **2**, 515-528.

39 M. V. Tsodikov, T. N. Rostovshchikova, V. V. Smirnov, O. I. Kiseleva, Y. V. Maksimov, I. P. Suzdalev, V. N. Ikorskii, *Catal. Today,* 2005, **105**, 634–640.

40 Q. Liu, W.M. Zhang, Z.M. Cui, B. Zhang, L.J. Wan, W.G. Song, *Micropor. Mesopor. Mater.,* 2007, **100**, 233–240.

41 X. Ma, X. Feng, J. Guo, H. Cao, X. Suo, H. Sun, M. Zheng, *Appl. Catal. B,* 2014, **147**, 666–676.

42 S. Krishnamoorthy, J. P. Baker, M. D. Amiridis, *Catalysis Today,* 1998, **40**, 39-46.

43 H. Y. Chang, S. P. Wang, J. R. Chang, H. S. Sheu, S. G. Shyu, *Appl. Catal. B,* 2012, **111-112**, 476-484.

44 B. H. Aristizabal, C. M. de Correa, A. I. Serykh, C. E. Hetrick, M. D. Amiridis, *J. Catal.,* 2008, **258**, 95-102.

45 S. Lomnicki, J. Lichtenberger, Z. Xu, M. Waters, J. Kosman, M. D. Amiridis, *Appl. Catal. B,* 2003, **46**, 105-119.

46 M. Kantcheva, A. S. Vakkasoglu, *J. Catal.,* 2004, **223**, 364-371.

47 X. Ma, H. Sun, H. He, M. Zheng, *Catal. Lett.,* 2007, **119**, 142-147.

Captions of the Figures:

Fig. 1. TGA curve of the as-prepared $Fe_{18}Ti_2O_x$ precursor.

Fig. 2. XRD diffraction patterns of the synthesized catalysts with different components: (■) peaks due to TiO_2-anatase; (●) peaks due to α-Fe_2O_3; (★) peaks due to γ-Fe_2O_3.

Fig. 3. Raman spectra of the synthesized catalysts with different components.

Fig. 4. (a) H_2-TPR profiles and (b) initial H_2 consumption rates of TiO_2, Fe_2O_3 and $Fe_{18}Ti_2O_x$.

Fig. 5. (a) Ti 2p XPS spectra and (b) O1s XPS spectra of prepared Fe_2O_3 and $Fe_{18}Ti_2O_x$.

Fig. 6. (a and b) Typical TEM images, (c) HRTEM image of $Fe_{18}Ti_2O_x$, and (d) selected area electron diffraction pattern of the $Fe_{18}Ti_2O_x$.

Fig. 7. (a) Nitrogen adsorption/desorption isotherms and (b) pore size distribution curve of $Fe_{18}Ti_2O_x$.

Fig. 8. Light-off curves for the oxidation of *o*-DCB over catalysts with different composition (100 ppm *o*-DCB, 10% O_2, balance N_2; GHSV=22,000 h^{-1}).

Fig. 9. Effect of different dosage of CTAB on the catalytic activity (100 ppm *o*-DCB, 10% O_2, balance N_2; GHSV=22,000 h^{-1}).

Fig. 10. The effect of oxygen concentration on the activity of $Fe_{18}Ti_2O_x$ (100 ppm *o*-DCB, 10% O_2, balance N_2; GHSV=22,000 h^{-1}).

Fig. 11. The stability tests of $Fe_{18}Ti_2O_x$ at 350°C (100 ppm *o*-DCB, 10% O_2, balance N_2; GHSV=22,000 h^{-1}).

Fig. 12. (a) Fe 2p, (b) C1s, (c) O1s and (d) Cl 2p XPS spectra of of the fresh and used $Fe_{18}Ti_2O_x$ (100 ppm *o*-DCB, 10% O_2, balance N_2; GHSV=22,000 h^{-1}).

Fig. 13. Plots of ln[1/(1-x)] vs. space time (τ) at different temperatures using $Fe_{18}Ti_2O_x$ (100 ppm *o*-DCB, 10% O_2, balance N_2; GHSV=22,000 h^{-1}).

Fig. 14. (a) In situ FTIR spectra of $Fe_{18}Ti_2O_x$ collected at 250°C after 1, 5, 10, 20 and 30min reaction and (b) at 200, 250 and 300°C after 10min reaction.

Fig. 15. Reaction mechanism for the oxidation of *o*-DCB over $Fe_{18}Ti_2O_x$ catalyst.

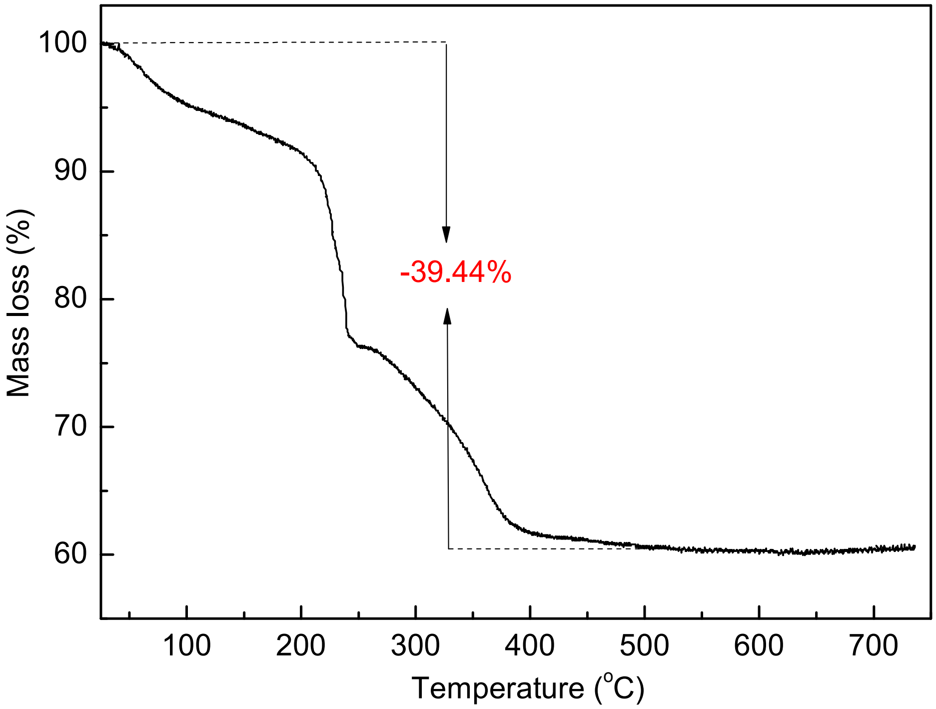

Fig. 1. TGA curve of the as-prepared $Fe_{18}Ti_2O_x$ precursor.

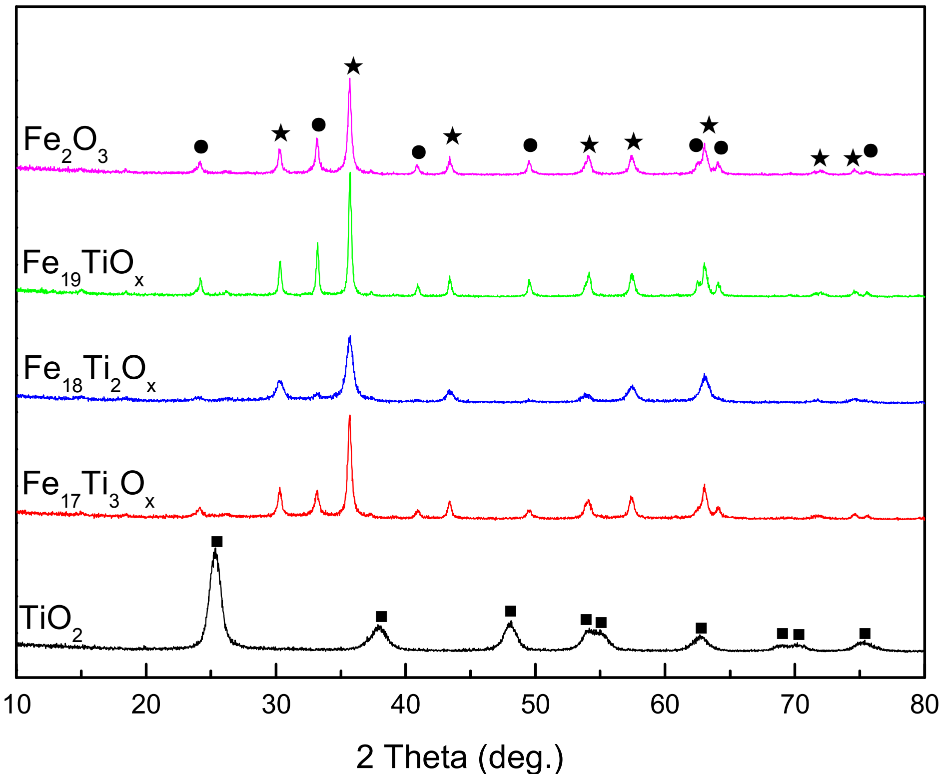

Fig. 2. XRD diffraction patterns of the catalysts with different components: (■) peaks due to TiO_2-anatase ; (●) peaks due to α-Fe_2O_3 ; (★) peaks due to γ-Fe_2O_3.

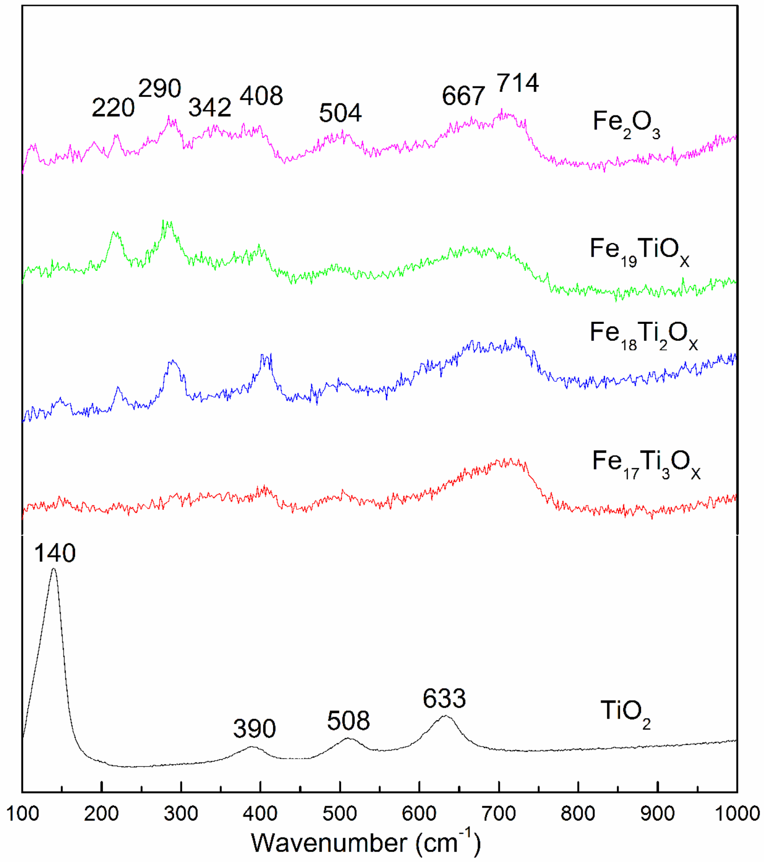

Fig. 3. Raman spectra of the synthesized catalysts with different components.

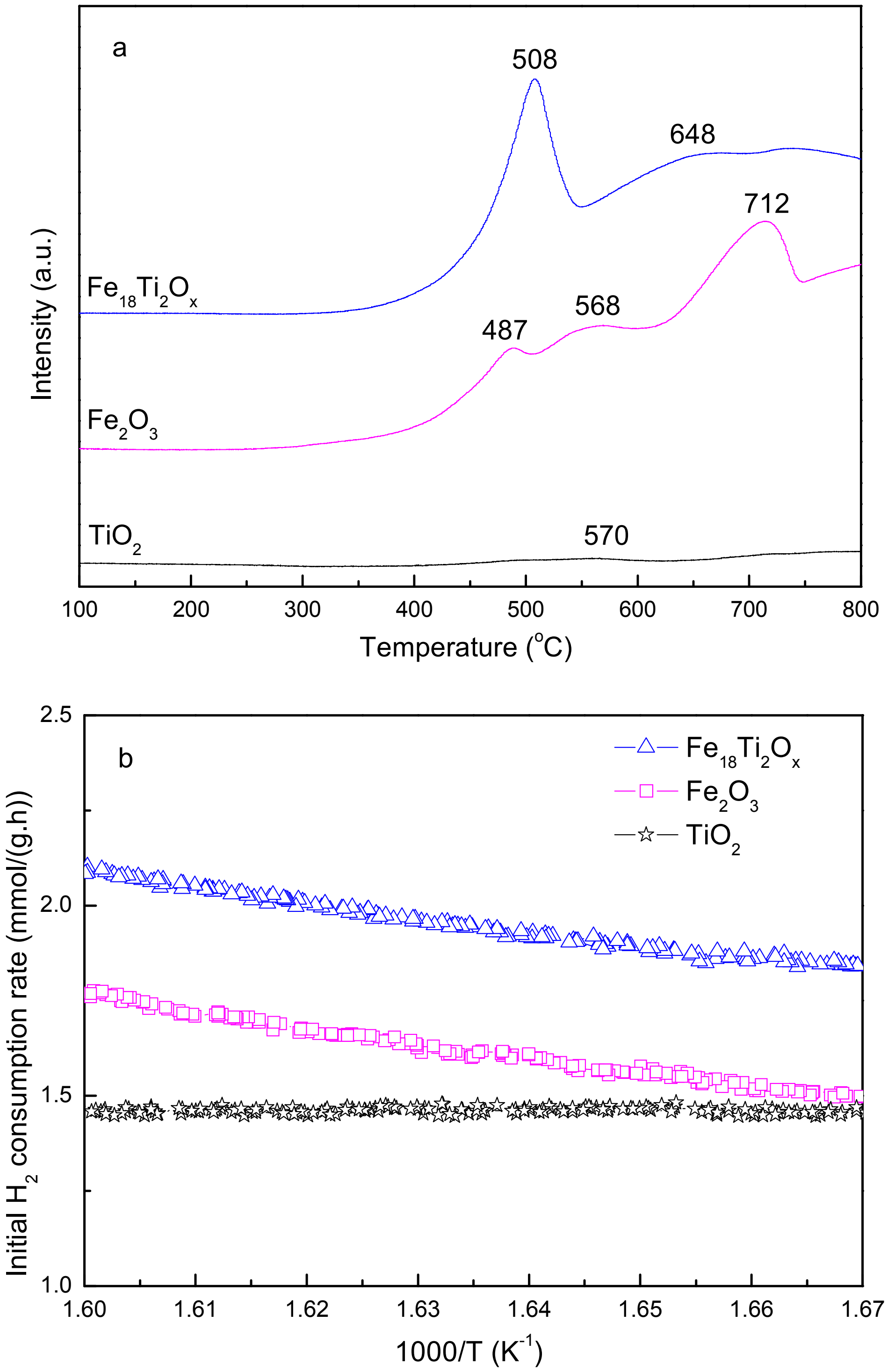

Fig. 4. (a) H_2-TPR profiles and (b) initial H_2 consumption rates of TiO_2, Fe_2O_3 and $Fe_{18}Ti_2O_x$.

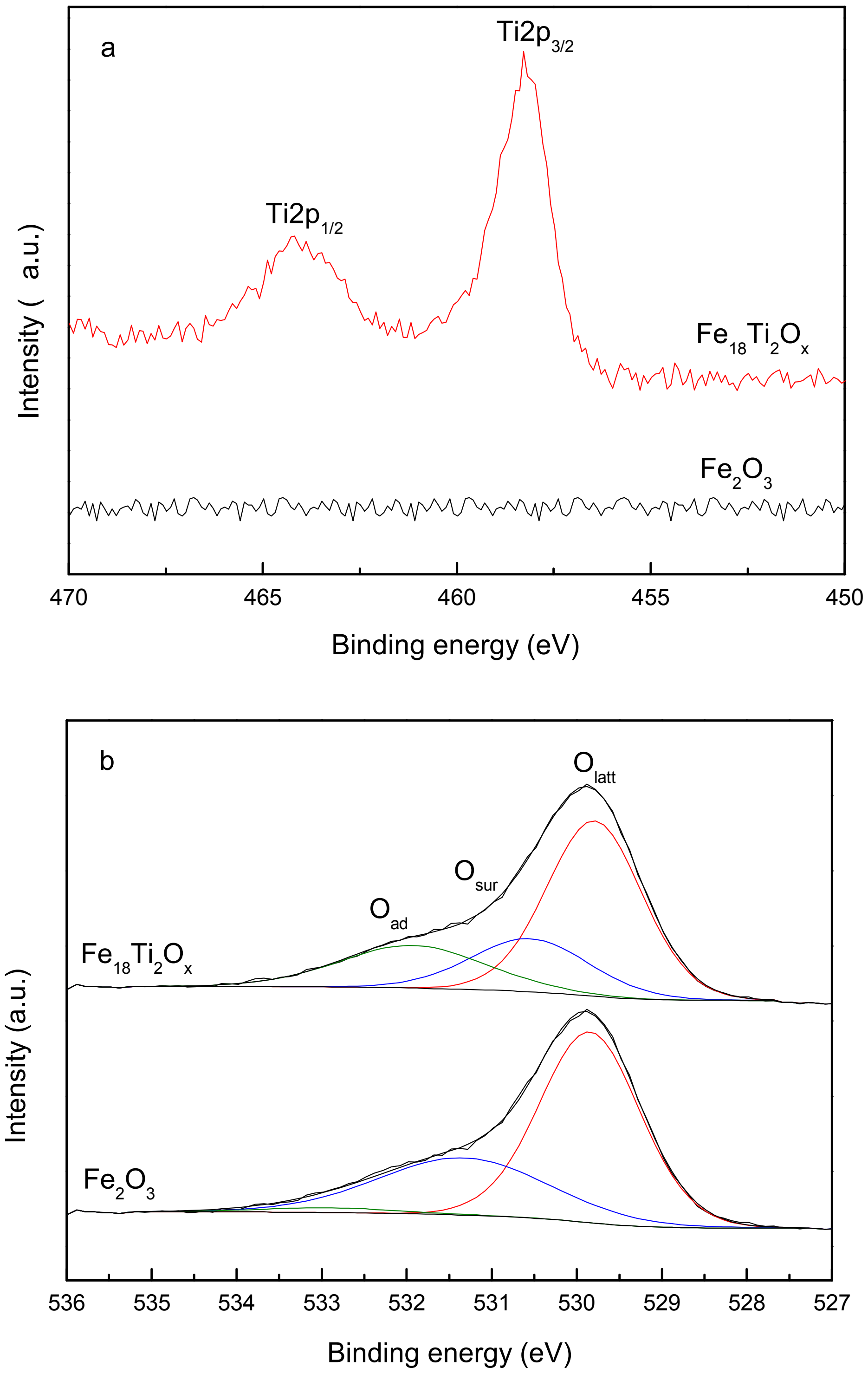

Fig. 5. (a) Ti 2p XPS spectra and (b) O1s XPS spectra of prepared Fe_2O_3 and $Fe_{18}Ti_2O_x$.

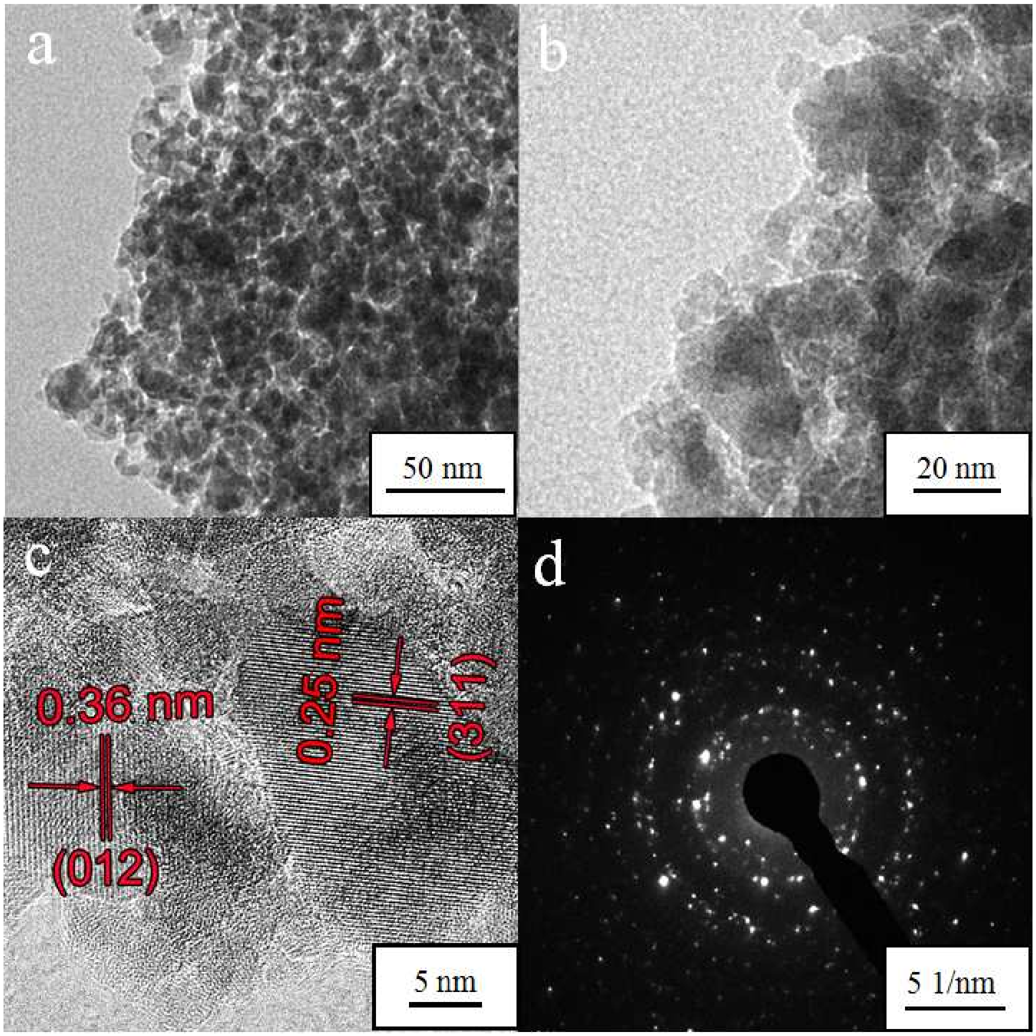

Fig. 6. (a and b) Typical TEM images, (c) HRTEM image of $Fe_{18}Ti_2O_x$, and (d) selected area electron diffraction pattern of the $Fe_{18}Ti_2O_x$.

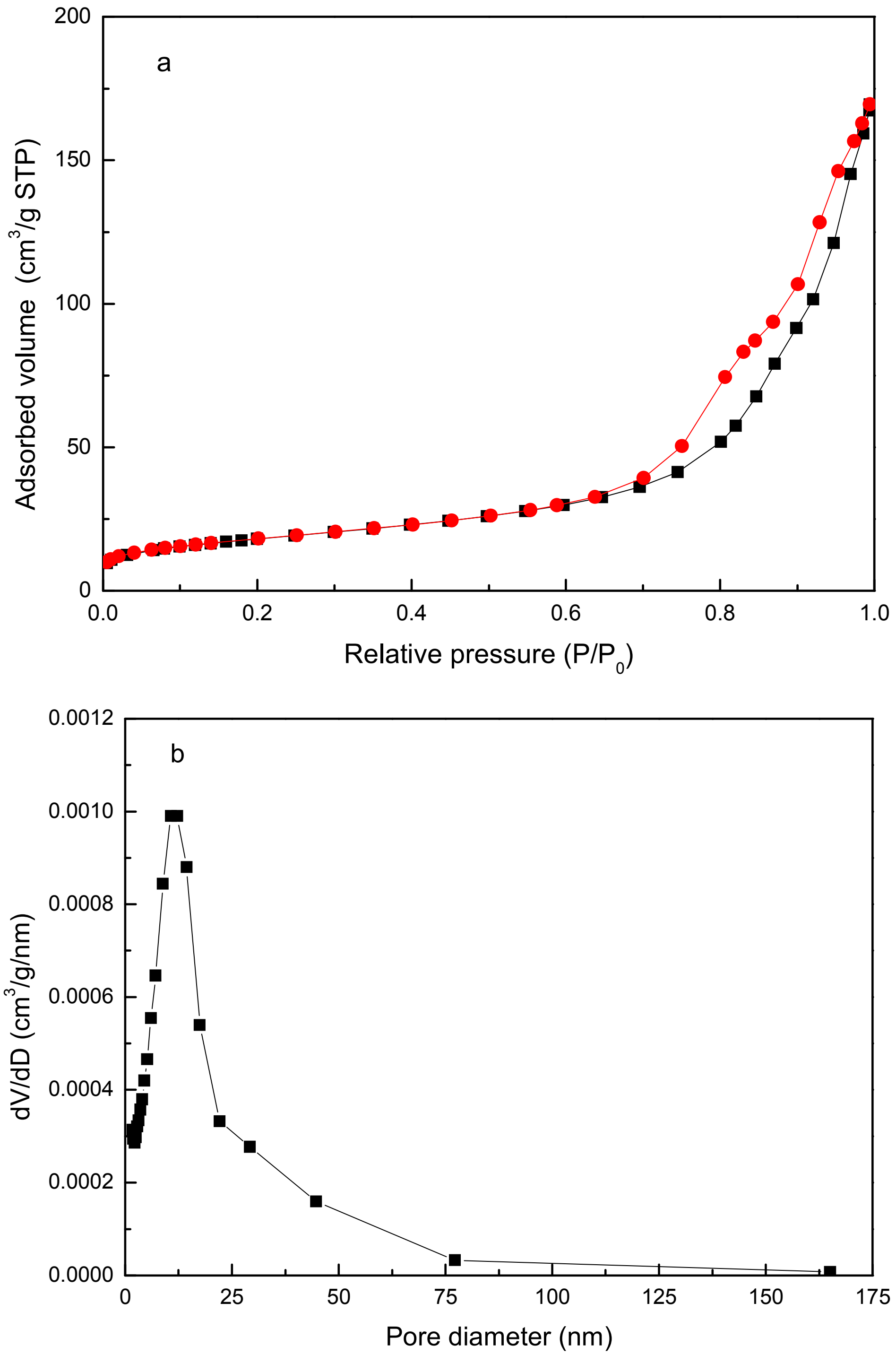

Fig. 7. (a) Nitrogen adsorption/desorption isotherms and (b) pore size distribution curve of $Fe_{18}Ti_2O_x$.

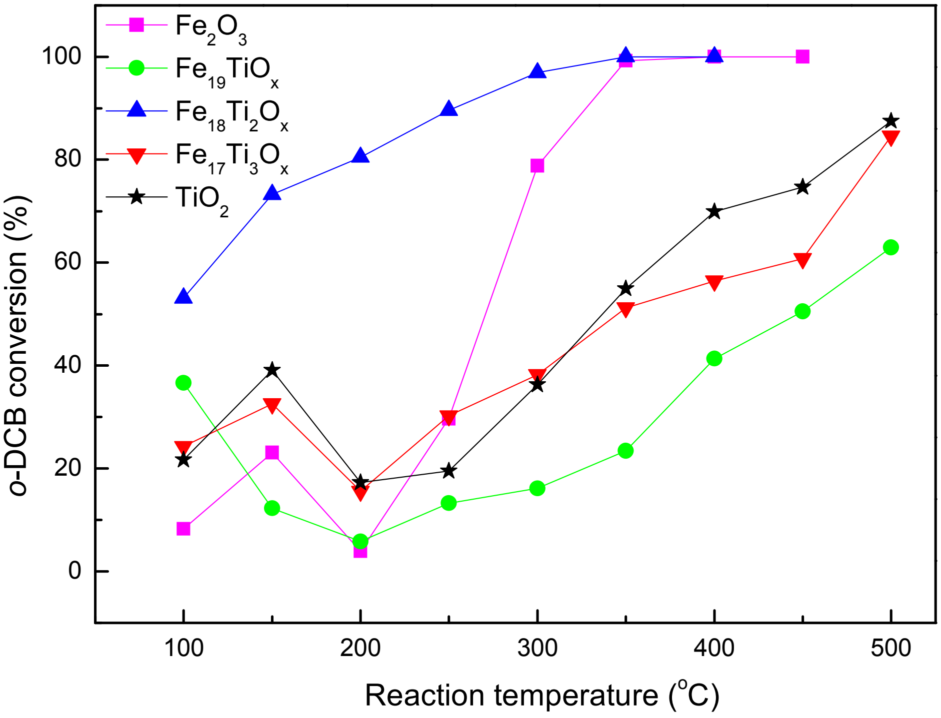

Fig. 8. Light-off curves for the oxidation of *o*-DCB over catalysts with different composition (100 ppm *o*-DCB, 10% O_2, balance N_2; GHSV=22,000 h^{-1}).

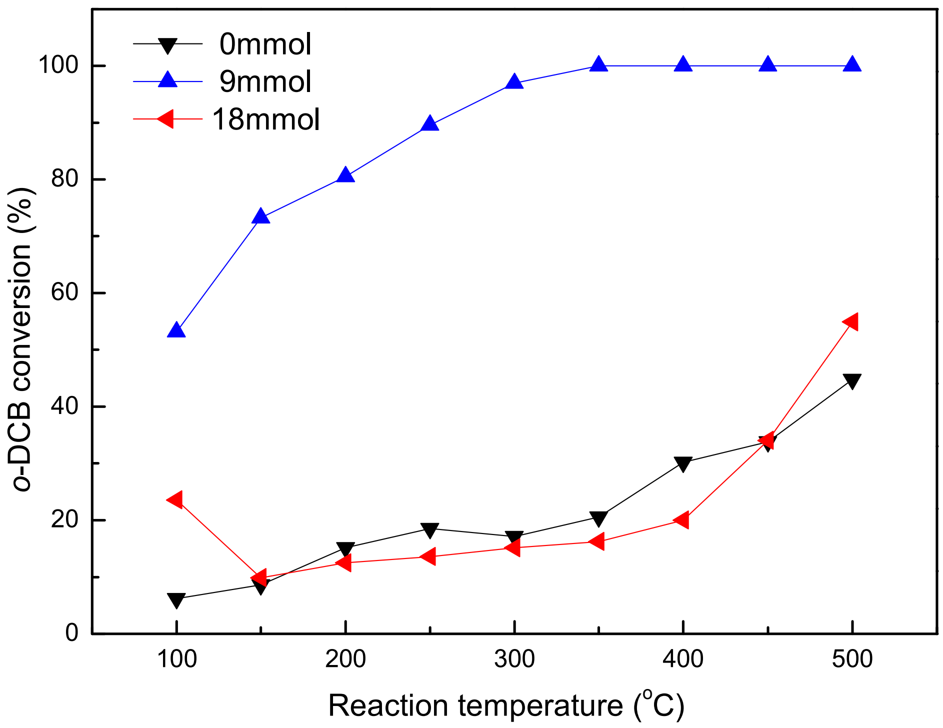

Fig. 9. Effect of different dosage of CTAB on the catalytic activity (100 ppm *o*-DCB, 10% O_2, balance N_2; GHSV=22,000 h^{-1}).

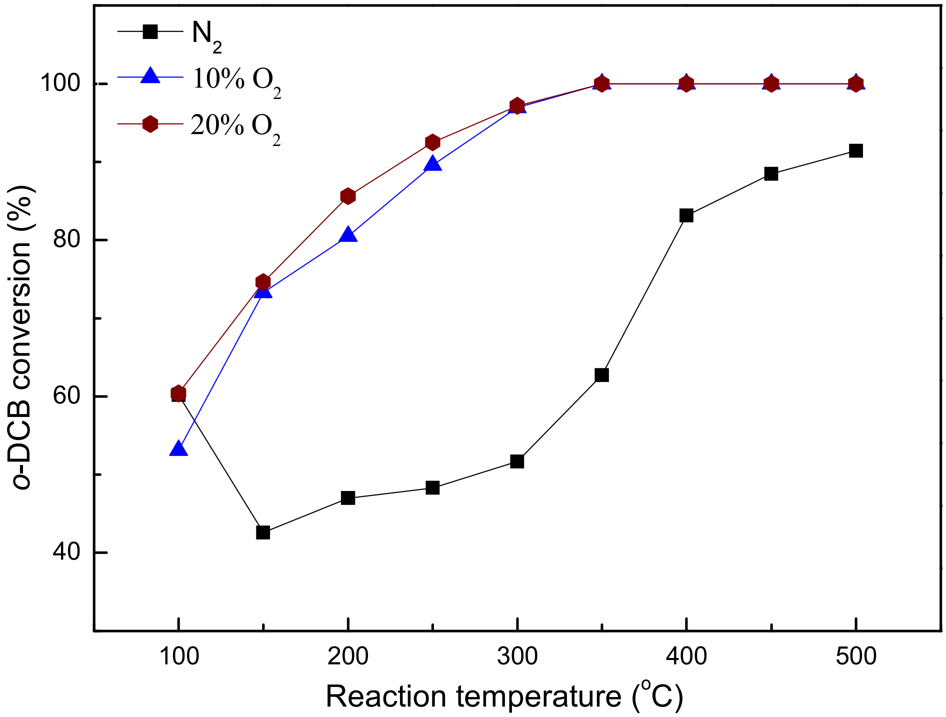

Fig. 10. The effect of oxygen concentration on the activity of $Fe_{18}Ti_2O_x$ (100 ppm *o*-DCB, 10% O_2, balance N_2; GHSV=22,000 h^{-1}).

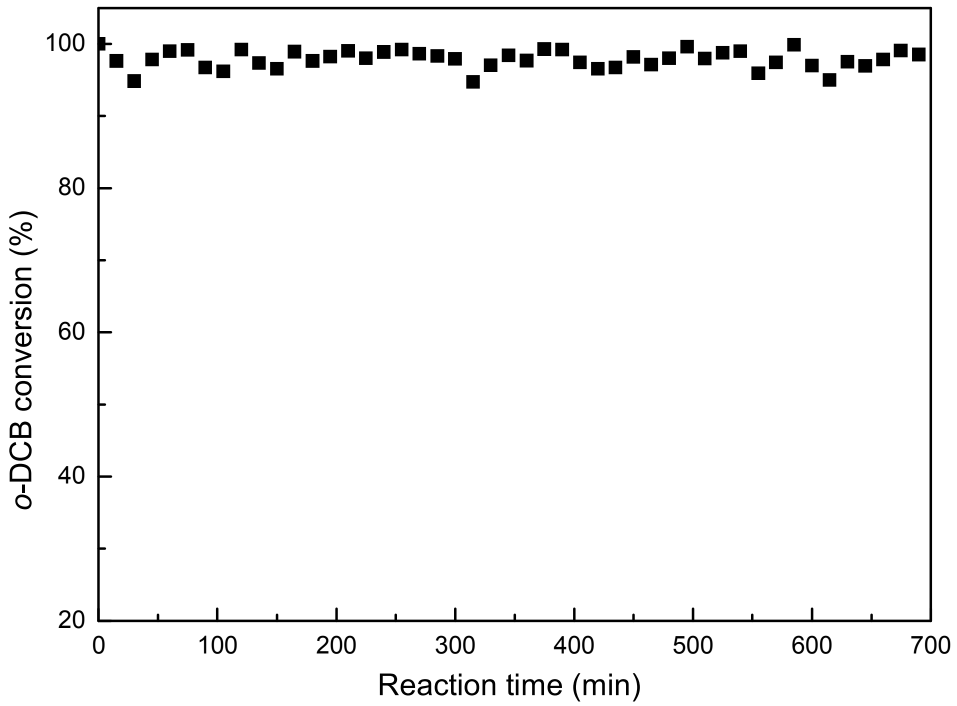

Fig. 11. The stability tests of $Fe_{18}Ti_2O_x$ at 350°C (100 ppm *o*-DCB, 10% O_2, balance N_2; GHSV=22,000 h^{-1}).

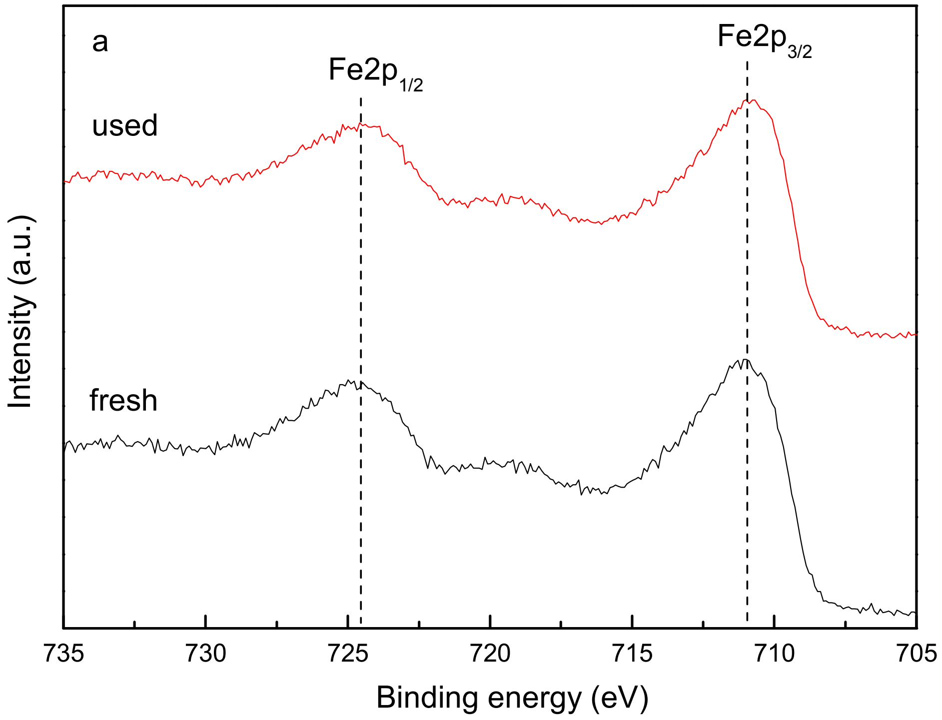
a
Fe2p$_{1/2}$
Fe2p$_{3/2}$
used
fresh
Intensity (a.u.)
735
730
725
720
715
710
705
Binding energy (eV)

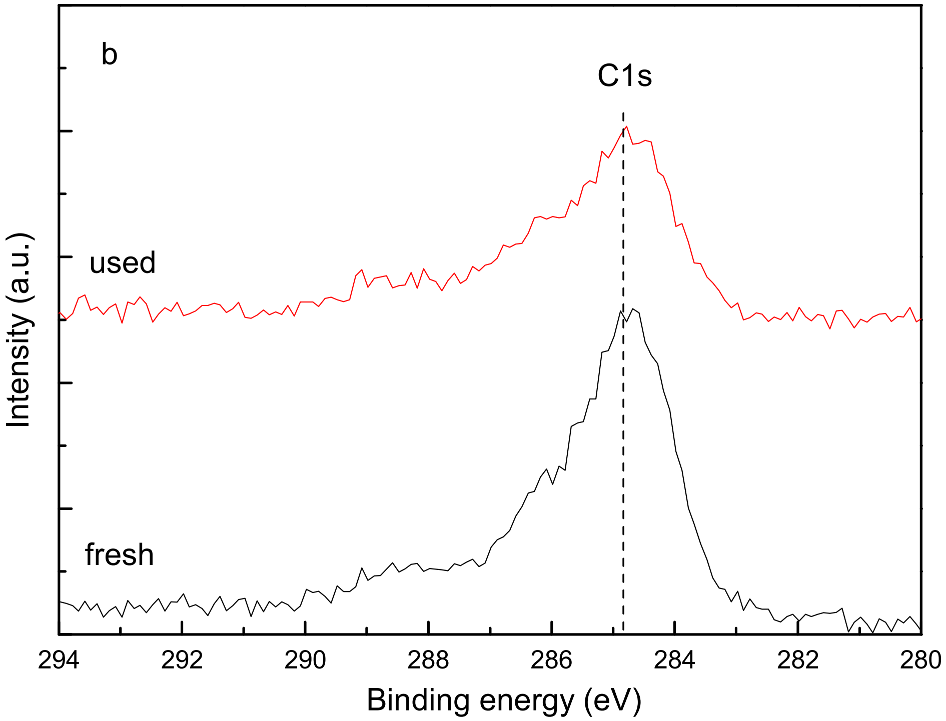
b
C1s
used
fresh
Intensity (a.u.)
294
292
290
288
286
284
282
280
Binding energy (eV)

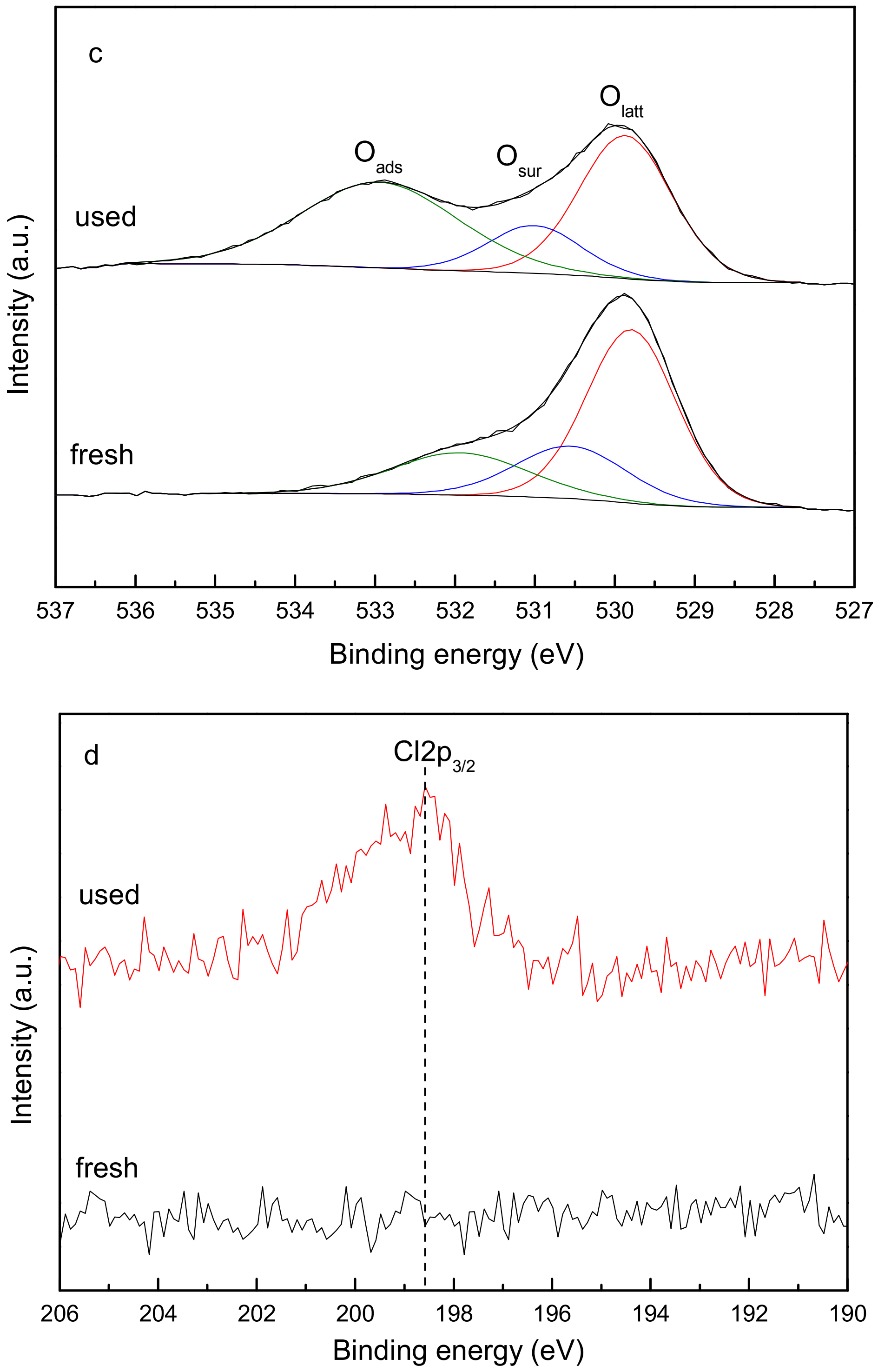

Fig. 12. (a) Fe 2p, (b) C1s, (c) O1s and (d) Cl 2p XPS spectra of of the fresh and used $Fe_{18}Ti_2O_x$ (100 ppm *o*-DCB, 10% O_2, balance N_2; GHSV=22,000 h^{-1}).

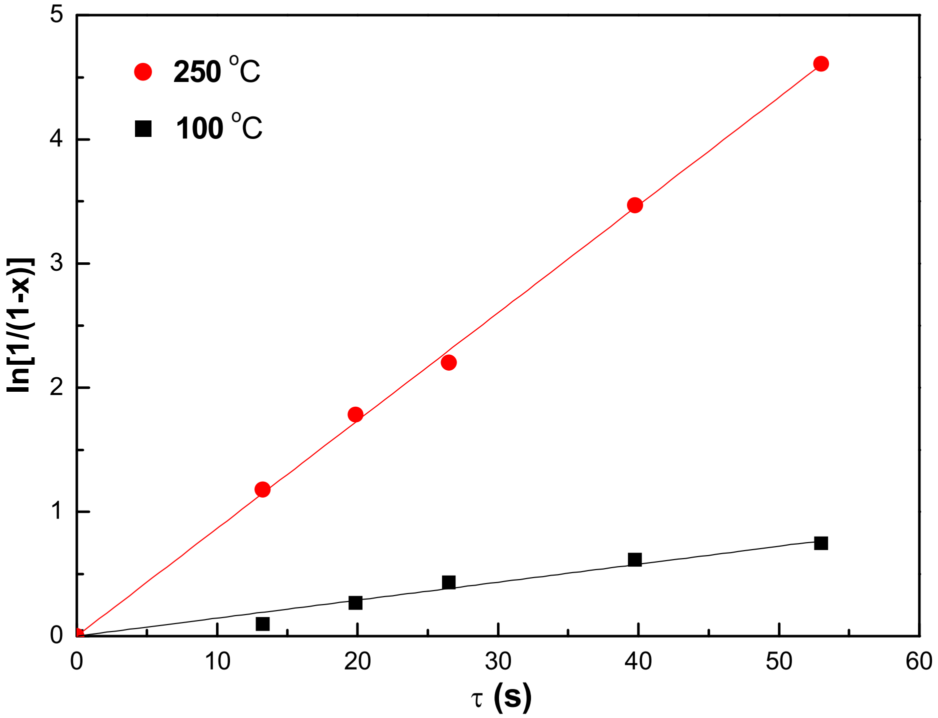

Fig. 13. Plots of ln[1/(1-x)] vs. space time (τ) at different temperatures using $Fe_{18}Ti_2O_x$ (100 ppm *o*-DCB, 10% O_2, balance N_2; GHSV=22,000 h^{-1}).

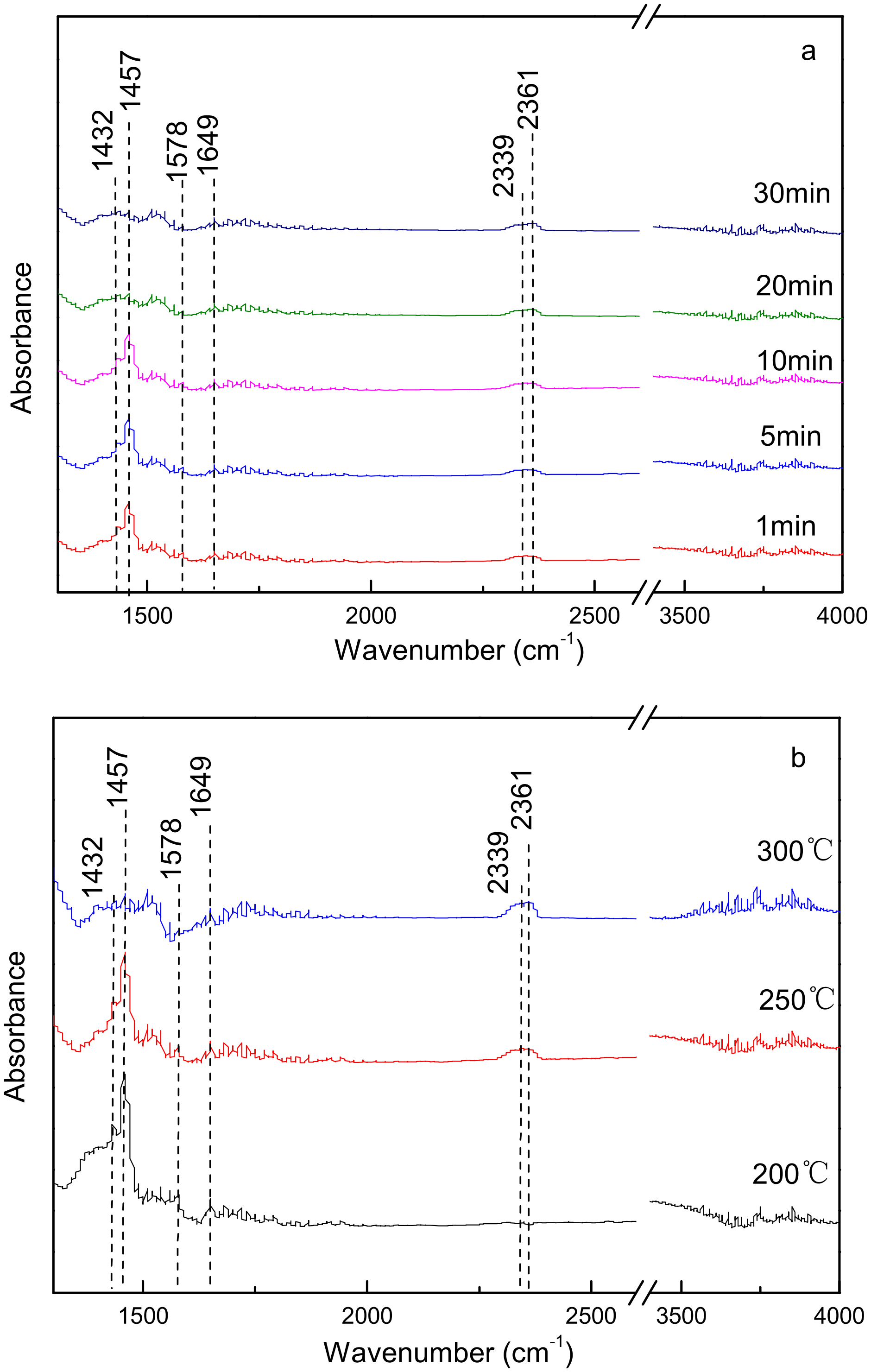

Fig. 14. (a) In situ FTIR spectra of $Fe_{18}Ti_2O_x$ collected at 250°C after 1, 5, 10, 20 and 30 min reaction and (b) at 200, 250 and 300°C after 10 min reaction.

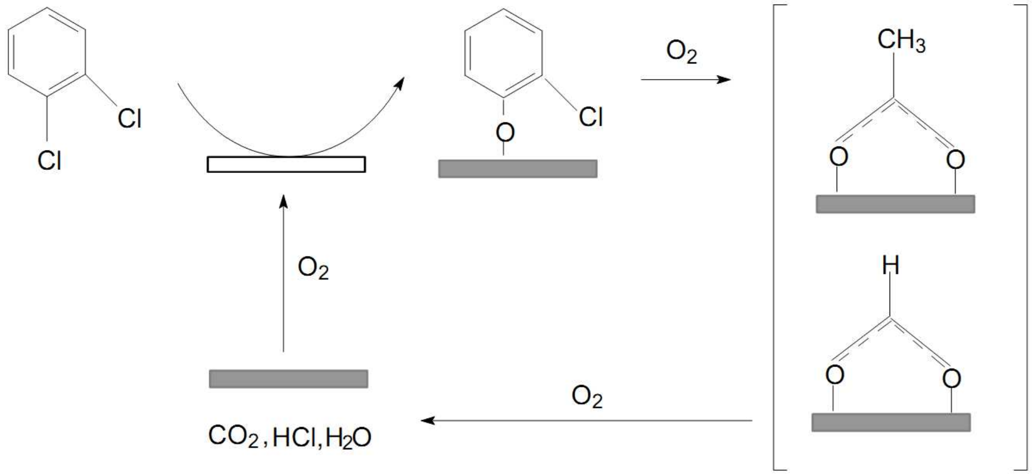

Fig. 15. Reaction mechanism for the oxidation of *o*-DCB over $Fe_{18}Ti_2O_x$ catalyst.